ELSEVIER

Experimental Thermal and Fluid Science 25 (2001) 383–396

Experimental Thermal and Fluid Science

www.elsevier.com/locate/etfs

Impingement cooling of a semi-cylindrical concave channel by confined slot-air-jet

N. Kayansayan *, S. Küçüka

Department of Mechanical Engineering, Dokuz Eylül University, Bornova 35100, Izmir, Turkey

Received 16 September 1999; accepted 18 July 2001

Abstract

An experimental and numerical study has been carried out for jet impingement cooling of a concave channel when the slot-jet was situated at the symmetry line of a semi-circular channel. In experiments, a parametric investigation is performed to measure the impingement surface pressure distributions and the local Nusselt numbers by varying the jet Reynolds number in the range from 200 to 11 000, and the slot-to-surface spacing from 2.2 to 4.2 of the slot width. For the range of Reynolds numbers studied, the heat transfer rates at the impingement surface of the concave channel are found to be more enhanced than the flat channel results due to the effect of channel curvature. A correlation for the stagnation region heat transfer, which accounts for the channel height effect, is presented. A numerical model, based on the finite-volume procedure, is constructed and validated by comparing the results with the experimental data at low Reynolds numbers. Due to large discrepancy between the experimental and the numerical results at high Reynolds numbers, however, the numerical analysis is carried out for flow Reynolds numbers up to 600.

Keywords: Heat transfer; Impingement cooling; Slot-jet; Two-dimensional; Numerical; Finite-volume; Concave; Semi-cylindrical; Experimental; Measurement

1. Introduction

Impingement cooling has been widely used to cool a heat transfer component exposed to a high temperature or a high heat flux environment. The impingement cooling jet has the advantage that it is readily moved to the location of interest and removes a large amount of heat. Jet impingement techniques have been applied to many industrial systems including high temperature gas turbines, paper drying, annealing of glassware, and high-density electronic equipment. The impingement jet used in these systems is air.

Over the past 30 years, impingement cooling heat transfer has been extensively studied. These studies include the impinging flow structure, local heat transfer, correlations of stagnation point and the average Nusselt numbers in terms of the relevant parameters. The structure of jets used in industrial applications is either axisymmetric or two-dimensional. The two-dimensional impingement cooling studied in the past was generally related to flat plate with a free jet [1] or a semi-confined jet(s) [2–4]. In contrast, studies related to impingement cooling over curved surfaces are relatively few. Metzger et al. [5] experimentally determined the impingement cooling heat transfer rates due to an array of round and free jets impinging on a concave surface. The studied geometry resembles the case of cooling the leading edge of a gas turbine airfoil. They measured the averaged heat transfer coefficient over the surface, and correlated the Nusselt number in terms of the jet Reynolds number, nozzle-to-plate spacing, and some additional parameters of the flow geometry. Brahma et al. [6], considering Walz's modification of the Karman–Pohlhausen integral method, presented a procedure for analyzing the boundary layer developed due to free-slot-jet impinging on a concave semi-cylindrical surface. An expression is derived to evaluate the thickness of the hydrodynamic boundary layer in terms of the jet exit velocity and the jet width. For the stagnation point heat transfer, a correlation has been presented in the form of $Nu_o = C\sqrt{Re}$, where the constant of proportionality is a function of the height ratio. Since the applied method provides results within the vicinity of the stagnation

* Corresponding author. Tel.: +90-232-388-3138; fax: +90-232-388-7868.

E-mail address: nuri.kayansayan@deu.edu.tr (N. Kayansayan).

0894-1777/01/$ - see front matter
PII: S0894-1777(01)00094-2

Nomenclature

a	a general coefficient in the finite-difference equations
A	surface area of a control-volume (m^2)
b	accumulated mass in a control-volume (dimensionless)
c_f	local skin friction coefficient (dimensionless)
h	local heat transfer coefficient ($W\ m^{-2}\ K^{-1}$)
H	non-dimensional channel height ($= z/l$)
k	thermal conductivity ($W\ m^{-1}\ K^{-1}$)
l	width of the slot-jet (m)
n,s,e,w	locations midway between grid nodes
N,S,E,W,P	finite-difference grid nodes
Nu	local Nusselt number ($= hl/k$)
p	pressure (Pa)
P	non-dimensional pressure ($= (p - p_\infty)/\ \rho u_1^2$)
P_r	reduced pressure (dimensionless)
r	radial coordinate from the center of the channel surface (m)
R	non-dimensional length in r-direction ($= r/l$)
R_*	radius ratio of the channel ($= R_2/R_1$)
Re	Reynolds number at the jet exit ($= U_1 l/\nu$)
S	source term (dimensionless)
T	temperature (K)
u	velocity component in r-direction ($m\ s^{-1}$)
U	non-dimensional velocity component in R-direction ($= u/U_1$)
v	velocity component in ϕ-direction ($m\ s^{-1}$)
V	non-dimensional velocity component in ϕ-direction ($= v/U_1$)
x	circumferential distance from the stagnation point (m)
X	non-dimensional distance from the stagnation point ($= x/l$)
Y	non-dimensional coordinate normal to the flow ($= y/l$)
z	distance between the jet exit and the impingement surface (m)

Greeks

α	relaxation factor
δ	difference
ϕ	coordinate in angular direction
φ	blow-angle
θ	non-dimensional temperature
μ	dynamic viscosity ($kg\ m^{-1}\ s^{-1}$)
ρ	density ($kg\ m^{-3}$)
σ	local stress ($N\ m^{-2}$)
ζ	surface curvature (m^{-1})

Subscripts

o	stagnation
n,s,e,w	directional locations on the control surface
N,S,E,W,P	finite-difference grid nodes
u	related to u-velocity component
v	related to v-velocity component
t	related to temperature
1	upper wall
2	impingement surface
∞	ambient

Superscripts

n,s,e,w	refers to directional locations
$\wedge$	refers to pseudo-values
$*$	refers to guessed values
$'$	refers to corrected values

point, the lateral variation of the thermal layer thickness is unpredictable in terms of the flow parameters. Moreover, the effect of surface curvature on heat transfer at the stagnation point is not considered by the presented method. Gau and Chung [7] performed experiments on two-dimensional free jet impinging normally on a concave and on a convex semi-cylindrical heated surface. Due to development of Taylor–Görtler vortices on the surface, they concluded that the increase in curvature increases the convective heat transfer along the concave surface. Yang et al. [8] experimentally studied the effect of slot nozzle configuration and curvature on impingement cooling of a semi-circular concave surface. Enhancement of heat transfer due to increase in curvature was also reported by this study.

As depicted in Fig. 1, the flow geometry of the present study consists of a semi-circular channel extended with a flat attachment at the tail zone. Air is injected through a slot that is located at the symmetry line of the upper wall. The symmetric flow and temperature conditions imposed at the slot-jet exit are taken into ac-

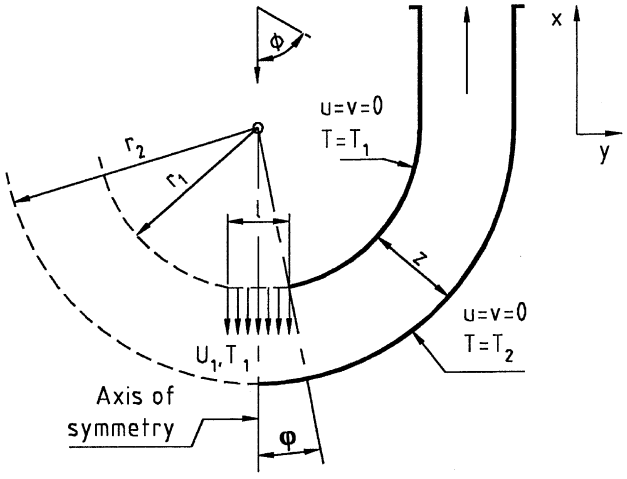

Fig. 1. Characteristic parameters of the flow geometry.

count in computations. A mathematical model is constructed for simulating the behavior of a semi-confined jet impinging on a two-dimensional and cylindrical channel. The fluid properties are assumed to be constant and the viscous dissipation is neglected. The slot width being the characteristic length, the flow Reynolds number, $U_1 l/v$, assumed values up to 600 in numerical analysis. Thus the flow and the heat transfer processes are considered to be laminar and steady. The following parameters describe the geometry of the flow: (1) the radius ratio, R_*, that is the ratio of radii of the lower to the upper wall, r_2/r_1, and (2) the non-dimensional channel height, H, that is the ratio of the channel height to the slot width, z/l. Varying the values of these parameters in the range between 1.5 and 5, a parametric study is carried out on the constructed model. Depending upon these parameters, the channel curvature at the upper wall is defined as follows:

$$\zeta_1 = \frac{1}{R_1} = \frac{R_* - 1}{H}. \quad (1)$$

In addition, as shown in Fig. 1, the blow-angle of the flow measures the angle between the symmetry line and the slot wall and is related to the flow geometry as follows:

$$\sin\varphi = \frac{R_* - 1}{2H}. \quad (2)$$

To verify the computational predictions of this study, an experimental set-up is designed and developed. A schematic of the experimental test section is illustrated in Fig. 2. Besides the jet Reynolds number, the test apparatus is capable of altering the height of the cylindrical channel. In experiments, the radius ratio spanned the range from 1.5 to 2.75, and the non-dimensional height from 2.2 to 4.2 accordingly.

As a consequence, the objectives of the present study are:

1. to simulate experimentally the flow of semi-confined slot jet impinging on a concave and heated surface and provide heat transfer data at low as well as at high Reynolds numbers;
2. to conduct a parametric study for investigating the effects of the geometry and the flow conditions on heat transfer characteristics;
3. to construct a mathematical model for predicting the laminar behavior of the flow, and validate the model by comparing the numerical predictions with the experimental data.

2. The experiments

2.1. The apparatus and the instrumentation

A schematic of the experimental apparatus is presented in Fig. 2 and an exploded view of the major components of the heat transfer section is given in Fig. 3. Air was supplied by the laboratory pressure-line facility at 7 bars and 21 °C and was carried from a rotameter exit to the system through a 2.5 cm flexible tubing. The rotameter had a sensitivity of 0.138 standard-m^3 per minute per cm of the bob displacement and was calibrated by the manufacturer, Schuette and Koerting, to be accurate within ±1% of the full range. A surge tank on the supply line separated the undesirable water particles from air.

The injection slot had the dimensions of 58 cm × 1.27 cm. A relatively large span length was necessary for simulating the two-dimensional flow. To assure a uniform velocity distribution along the slot exit, the air-plenum was furnished with eight divergent nozzles at the inlet, and with a flow straightener unit at a region close to the plenum exit. After a calibration process, a maximum of 4% deviation in the velocity at the slot exit was noticed and considered to be adequate for two-dimensional flow simulation. The impingement wall of the channel was made of 5 mm thick steel with 84 mm of inner radius of curvature. The out of roundness of the steel shell was less than ±0.01 mm with a surface roughness of 0.75 μm. The channel top cover and the sidewalls were made of Plexiglas. The entire system was placed on a styrofoam support that was covered with a heat-resistant fiberglass liner.

To determine the static pressure distribution on the impingement surface, the static tap holes 0.5 mm in diameter were drilled along the circumference of the shell. Because of the steep change of pressure around the stagnation, the tap holes close to this region were placed closer together than the ones at large distances from the stagnation point. The pressure signals were transmitted through Teflon tubings to a rotary switch and a pressure transducer measured the pressure inputs at the switch. Depending upon the selected range multiplier, the electronic manometer, Barocel type 1173, provided a readability access ranging from 10^{-5} to 10 mm Hg. The manufacturer, Datametric, specified the accuracy of the complete set as ±0.1% of the reading.

To achieve a uniform temperature at the impingement surface, a total of nine heating strips with the dimensions of 58 cm × 2.5 cm were used to regulate the electric power inputs. The power input to the heating elements except the one at the stagnation was controlled by an RCA type proportional-temperature-controller which was activated by eight thermistors embedded in the impingement wall of the test section. Each thermistor was part of a bridge providing a temperature feedback to the controller. The power input of the stagnation strip, however, was controlled manually by an auto-transformer. An AC voltage regulator that regulated a 230-V line source with ±1% uncertainty supplied power to the system. A calibrated wattmeter measured the power inputs of the heating strip. As shown in Fig. 3, four moveable rings with a cross-section of 16.5 mm × 2.5 mm and flush with the impingement surface (the concave surface of the shell) were used for collecting the circumferential heat transfer data. A thermal compound was used for reducing the thermal contact resistance between the sliding surfaces of the rings and the shell. A total of four micro-foil heat flow

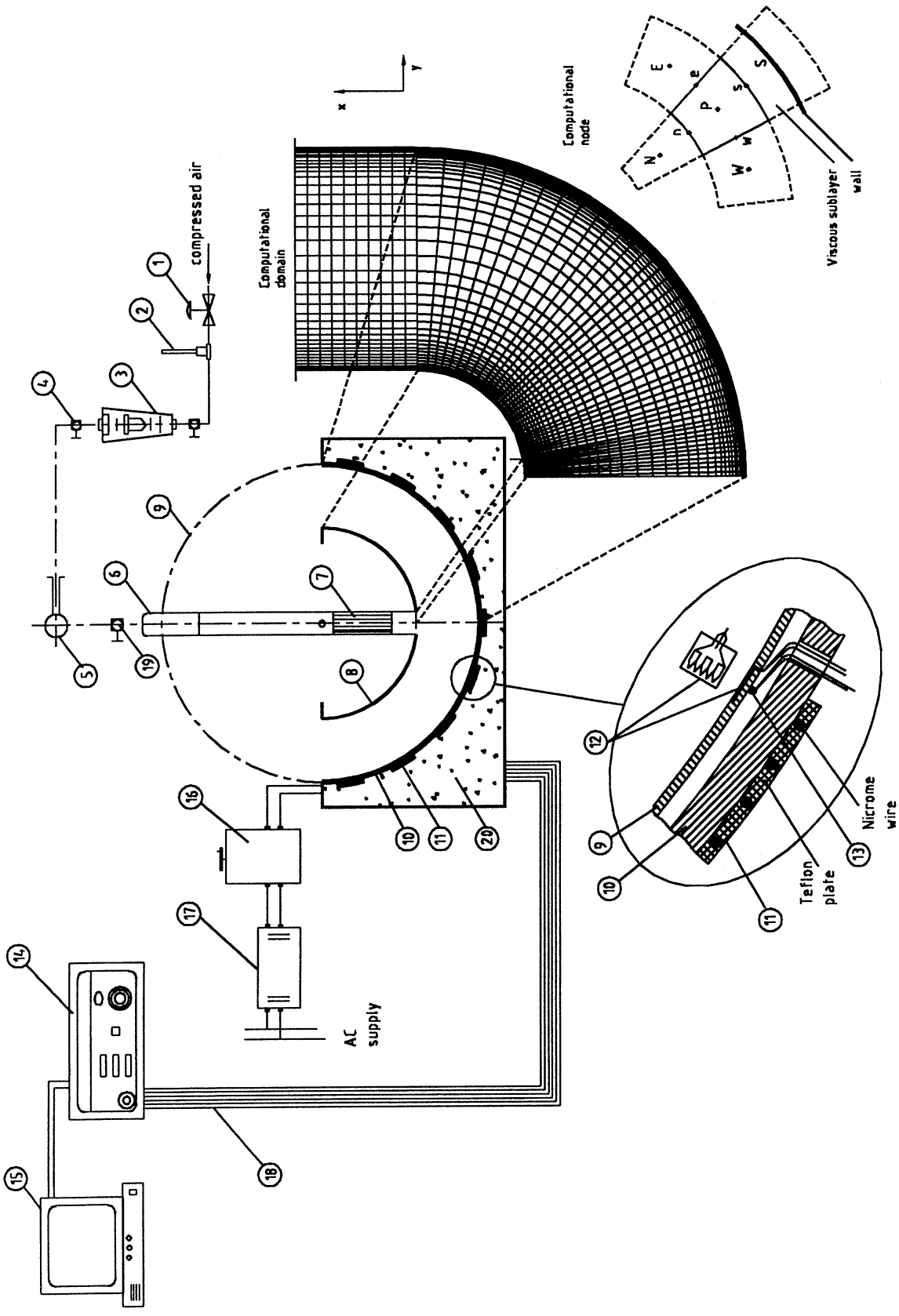

Fig. 2. Schematic of the experimental apparatus and the computational domain. 1: Main valve; 2: well-type thermometer; 3: rotameter; 4: flow adjustment valve; 5: central manifold; 6: air-plenum; 7: straightener; 8: upper wall; 9: ring; 10: impingement surface; 11: heating strip; 12: heat flow sensor; 13: T-type thermocouple, 14: data logger; 15: PC computer; 16: auto-transformer; 17: AC voltage regulator; 18: thermocouple and heat flow extension wires; 19: valves for uniform velocity distribution; 20: insulation.

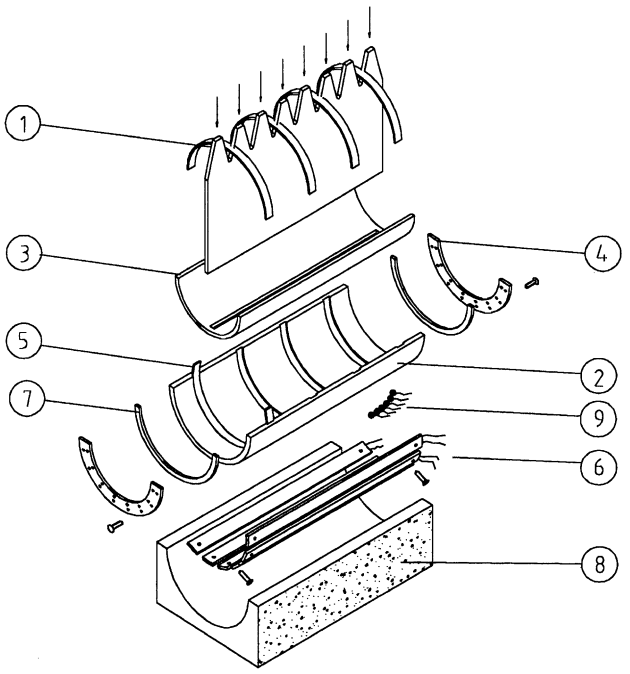

Fig. 3. An exploded view of the major components of heat transfer section. 1: Air-plenum; 2: impingement surface; 3: upper wall; 4: side wall; 5: data collecting ring; 6: heating strip; 7: end face insulation; 8: insulation; 9: thermistor.

sensors, each having an active area of 15 mm × 15 mm and a nominal sensitivity of 2.9 mV/(W/cm^2) at 21 °C of temperature, were bonded on the milled recesses of the rings facing the air jet. The heat flow sensors were calibrated by the manufacturer, RDF, by using a radiation source, and measured the local heat flux within ±3% accuracy. A copper–constantan thermocouple affixed to the underside of each of the heat flow sensor-monitored the temperature of the heat transfer surface. A HP type 34970A data logger that had an accuracy of ±0.04% of the reading measured the millivolt outputs of thermocouples and heat flow sensors. Through RS232 type connection, the signal outputs of the data logger were transmitted and recorded in a personal computer. A typical temperature variation along the heated surface was observed to be ±2 °C with the overall temperature differential between the heated shell and the injected air at 40 °C; this was equivalent to a ±5% temperature variation from isothermal condition.

2.2. The experimental procedure

The heat transfer between the impinging air jet and the channel surface, as well as the surface pressure variation, was measured for various flow rates and for three different channel heights, namely $z = 27.9$, 40.6, and 53.3 mm. As the channel height changed, the radius of the upper wall was varied accordingly so that both surfaces shared a common center of curvature. For each run, the airflow rate was set to a desired value. The impingement surface was then heated to a temperature of 62 °C, and this temperature was kept constant during the experimentation. The bob level of the rotameter, the rotameter upstream static pressure, and the injected air temperature were recorded. The barometric pressure of the room was registered for accurate mass flow rate calculations. In recording the static pressure at each port, a sufficient time was allowed for the electronic manometer indicator to reach equilibrium. Hence the pressure output was determined as

$$p = (10)(E)(RX), \tag{3}$$

where E is the analog output in mm-Hg and RX is the range multiplier of the manometer.

Positioning the heat flow sensor of the data-collecting ring at the stagnation point, the heat flux and the wall temperature were measured. Then the rings were moved to a new location with an incremental step of $X = 0.25$. Thus an arc length spanning the range $0 \leqslant X \leqslant 10$ was covered in experiments. The heat flux recorded at different axial positions by four data collecting rings was averaged to give mean values. The maximum deviation of any of the individual heat flux readings from the average value was ±10%. Due to finite thermal resistance between the points of thermocouple installation and the impingement surface, a correction was made to take this resistance into account in determining the heat transfer coefficients. The local heat transfer coefficient was calculated accordingly as

$$h = \frac{(K_t)(e)}{(K)(T_2 - T_1)}, \tag{4}$$

where K_t is the temperature correction for the sensor output of e millivolts and K represents the sensor sensitivity in millivolts per W/m^2. Prior to changing the jet flow rate, the power consumed by the strip at the stagnation region was recorded. In experiments, the jet Reynolds number was varied in the range between 200 and 11 000. After collecting the data for the entire range of Reynolds numbers, the channel height was altered to a new value with a process of replacing the Plexiglas upper and side walls, and the data-recording procedure was repeated.

The uncertainty in the Reynolds number especially at low flow rates was within ±10% and in pressure measurements at the impingement surface was about ±1%. The uncertainties in the experimental heat transfer coefficients were found to be of the order of 6%. The experimental results were reproducible within these uncertainty ranges.

3. Mathematical modeling

The mathematical model employs a control-volume finite-difference method for discretizing the momentum and energy equations. In Fig. 4, a typical computational cell enclosing the node P and obtained by the orthogonal intersecting lines drawn in R and ϕ directions is

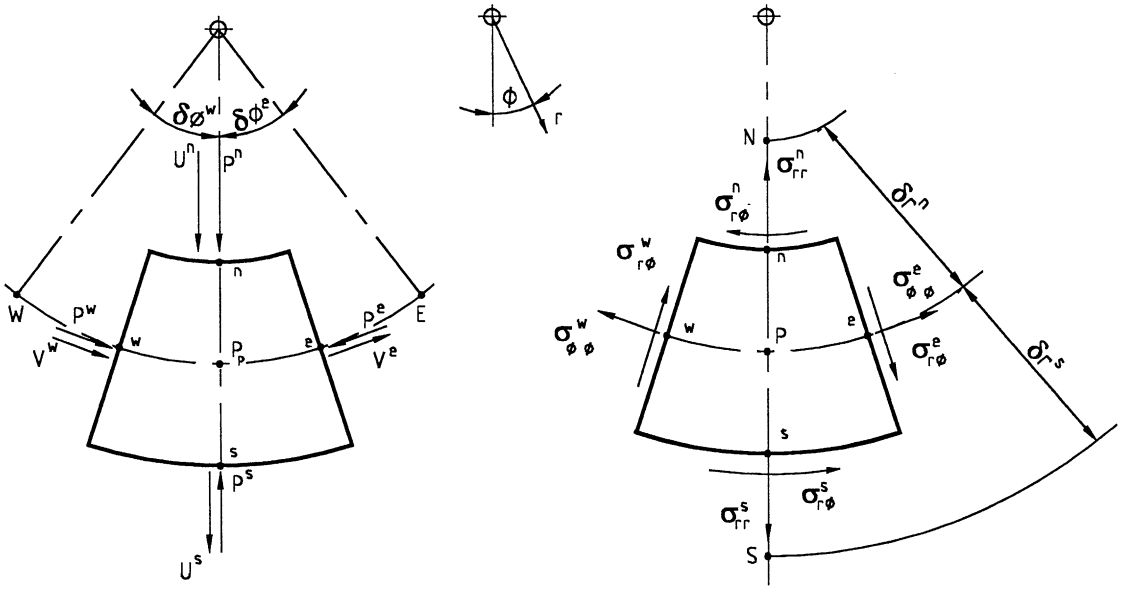

Fig. 4. A typical finite-difference grid in cylindrical coordinate showing the location of variables and stresses around the node P.

illustrated. The point P, the central node, has four neighboring nodes N, S, E, and W at which the pressure and temperature values are stored. On the other hand, the velocity components are calculated and stored in the cell faces identified by n, s, e, and w which are at midpoints between these grid nodes. This grid arrangement is known as the staggered-grid system.

The grid spacing need not necessarily be uniform for the entire solution domain. A fine grid spacing was applied to regions where steep change in velocities or in temperature was expected. In all configurations, the radial grid size was varied so as to provide a finer grid near the lower and the upper walls. For grid distribution in the angular direction, the intensive flow field in the vicinity of the symmetry axis is identified by the blow-angle φ. Thus the flow region between the axis of symmetry and the blow-angle is traced by equally spaced grids with an angular increment, $\Delta\phi$, being in the vicinity of 0.1° and this angular increment remains constant for the first two flow regions. The next equally spaced grids with an increment size 5% greater than the previous size define the third computational region in the ϕ-direction. A total of 14 computational zones are defined in the angular direction. Starting from the third zone, the mesh size is sequentially increased by 5%, 10%, and 15% of the preceding, and the remaining zones shared the same mesh size as that obtained at the fifth domain. Throughout the computations, the magnitude of the angle ϕ is checked for values greater than 90°. A coordinate transformation is applied to governing equations in the vicinity of $\phi = 90°$ and appropriate increments in Cartesian coordinate system are specified as, $\delta X_i = R_1\delta\phi_i$, and $\delta Y_j = R_{j+1} - R_j$. In the analysis, the outflow boundary is assured to be sufficiently far from the impingement region. Then the flow conditions at the channel exit are considered to be fully developed with zero velocity component in the radial direction.

3.1. The governing equations in discretized form

As depicted in Fig. 4, relating the value of a velocity component at node P to those at nodes N, S, E, and W, the following equations of motion may be derived by considering the balance of forces over the control surface of the finite-difference cell. Thus, in r-direction:

$$\rho\Big\{\big[(vv)_{\mathrm{e}} - (vv)_{\mathrm{w}}\big]\delta r + \big[(ruv)_{\mathrm{s}} - (ruv)_{\mathrm{n}}\big]\delta\phi + (uv)_{\mathrm{p}}\delta r\delta\phi\Big\} = (p_{\mathrm{w}} - p_{\mathrm{e}})\delta r + \big[(\sigma_{r\phi}r)_{\mathrm{s}} - (\sigma_{r\phi}r)_{\mathrm{n}}\big]\delta\phi + \big(\sigma_{\phi\phi,\mathrm{e}} - \sigma_{\phi\phi,\mathrm{w}}\big)\delta r + \sigma_{r\phi,\mathrm{p}}\delta r\delta\phi \tag{5}$$

and in ϕ-direction:

$$\rho\Big\{\big[(vv)_{\mathrm{e}} - (vv)_{\mathrm{w}}\big]\delta r + \big[(ruv)_{\mathrm{s}} - (ruv)_{\mathrm{n}}\big]\delta\phi + (uv)_{\mathrm{p}}\delta r\delta\phi\Big\} = (p_{\mathrm{w}} - p_{\mathrm{e}})\delta r + \big[(\sigma_{r\phi}r)_{\mathrm{s}} - (\sigma_{r\phi}r)_{\mathrm{n}}\big]\delta\phi + (\sigma_{\phi\phi,\mathrm{e}} - \sigma_{\phi\phi,\mathrm{w}})\delta r + \sigma_{r\phi,\mathrm{p}}\delta r\delta\phi. \tag{6}$$

In regard to viscous stresses for Newtonian fluids [9], the differential forms of velocities at boundary surfaces are expressed in terms of the velocities at nodes and the stresses are determined to be as follows:

$$\sigma^{\mathrm{s}}_{rr} = 2\mu\frac{U_{\mathrm{S}} - U_{\mathrm{P}}}{\delta r^{\mathrm{s}}},$$

$$\sigma^{\mathrm{n}}_{rr} = 2\mu\frac{U_{\mathrm{P}} - U_{\mathrm{N}}}{\delta r^{\mathrm{n}}},$$

$$\sigma^{\mathrm{e}}_{r\phi} = \mu\left[\frac{r_{\mathrm{p}}}{\delta r}\left(\frac{V^{\mathrm{se}}}{r^{\mathrm{s}}} - \frac{V^{\mathrm{ne}}}{r^{\mathrm{n}}}\right) + \frac{1}{r_{\mathrm{p}}}\frac{U_{\mathrm{E}} - U_{\mathrm{P}}}{\delta\phi^{\mathrm{e}}}\right],$$

$$\sigma^{\mathrm{w}}_{r\phi} = \mu\left[\frac{r_{\mathrm{p}}}{\delta r}\left(\frac{V^{\mathrm{sw}}}{r^{\mathrm{s}}} - \frac{V^{\mathrm{nw}}}{r^{\mathrm{n}}}\right) + \frac{1}{r_{\mathrm{p}}}\frac{U_{\mathrm{P}} - U_{\mathrm{W}}}{\delta\phi^{\mathrm{w}}}\right],$$

$$\sigma^{\mathrm{n}}_{r\phi} = \mu\left[\frac{V_{\mathrm{P}} - V_{\mathrm{N}}}{\delta r^{\mathrm{n}}} - \frac{V^{\mathrm{n}}}{r^{\mathrm{n}}} + \frac{1}{r^{\mathrm{n}}}\frac{U^{\mathrm{ne}} - U^{\mathrm{nw}}}{\delta\phi}\right],$$

$$\sigma^{s}_{r\phi} = \mu\left[\frac{V_S - V_P}{\delta r^s} - \frac{V^s}{r^s} + \frac{1}{r^s}\frac{U^{se} - U^{sw}}{\delta\phi}\right],$$
$$\sigma^{e}_{\phi\phi} = \frac{2\mu}{r_p}\left[\frac{V_E - V_P}{\delta\phi^e} + U^e\right],$$
$$\sigma^{w}_{\phi\phi} = \frac{2\mu}{r_p}\left[\frac{V_P - V_W}{\delta\phi^w} + U^w\right], \quad (7)$$
$$\sigma_{r\phi,p} = \mu\left[\frac{V^s - V^n}{\delta r} - \frac{V_P}{r_p} + \frac{1}{r_p}\frac{U^e - U^w}{\delta\phi}\right],$$
$$\sigma_{\phi\phi,p} = \frac{2\mu}{r_p}\left[\frac{V^e - V^w}{\delta\phi} + U_P\right].$$

Eq. (7) is substituted into Eqs. (5) and (6), and the following non-dimensional quantities are used in the derivations:

$$R = r/l, \quad U = u/U_1, \quad V = v/U_1,$$
$$Re = \frac{\rho U_1 l}{\mu}, \quad P = \frac{p - p_\infty}{\rho U_1^2}. \quad (8)$$

Thus the equations of motion in r and ϕ directions are transformed into the following algebraic equations:

r-direction:

$$a^n_u U_N + a^s_u U_S + a^e_u U_E + a^w_u U_W = a_{pu} U_P + R_p(P_n - P_s)\delta\phi + S_u, \quad (9)$$

ϕ-direction:

$$a^n_v V_N + a^s_v V_S + a^e_v V_E + a^w_v V_W = a_{pv} V_P + (P_w - P_e)\delta R + S_v. \quad (10)$$

The source terms S_u and S_v in these equations are linearized and presented in terms of the velocity components of node P as follows:

$$S_u = S_{cu} + S_{pu} U_P,$$
$$S_v = S_{cv} + S_{pv} V_P, \quad (11)$$

where the coefficients S_c and S_p are determined to be as follows:

$$S_{pu} = \frac{2\delta R\delta\phi}{Re\, R_p},$$
$$S_{pv} = \left[\frac{1}{Re\, R_p} + \|U_P, 0\|\right]\delta R\delta\phi,$$
$$S_{cu} = \frac{R_P}{Re}\left(\frac{V^{ne} - V^{nw}}{R^n} - \frac{V^{se} - V^{sw}}{R^s}\right) + \frac{2(V^e - V^w)}{Re\, R_P}\delta R - V_P^2\delta R\delta\phi, \quad (12)$$
$$S_{cv} = \frac{1}{Re}[(U^{ne} - U^{nw}) - (U^{se} - U^{sw})] - \frac{3(U^e - U^w)}{Re\, R_P}\delta R + V_P\|-U_P, 0\|\delta R\delta\phi.$$

In addition to the conservation of momentum in both directions of U and V, the conservation of mass requires that the tangential velocity component V at a particular grid nodes satisfy the continuity relation as follows:

$$V^e = V^w + [R_n U^n - R_s U^s]\frac{\delta\phi}{\delta R}. \quad (13)$$

Similarly, neglecting the viscous dissipation term, the non-dimensional energy equation in cylindrical coordinates is as follows:

$$U\frac{\partial\theta}{\partial R} + \frac{V}{R}\frac{\partial\theta}{\partial\phi} = \frac{1}{RePr}\left[\frac{1}{R}\frac{\partial}{\partial R}\left(R\frac{\partial\theta}{\partial R}\right) + \frac{1}{R^2}\frac{\partial^2\theta}{\partial\phi^2}\right], \quad (14)$$

where the non-dimensional temperature is defined as

$$\theta = \frac{T - T_1}{T_2 - T_1}. \quad (15)$$

Multiplying both sides of Eq. (14) by $R\,dR\,d\phi$ and integrating over the control surface of Fig. 4, and rearranging yield the following discretized relation among the temperatures of computational cells surrounding the node P:

$$a^n_t\theta_N + a^s_t\theta_S + a^e_t\theta_E + a^w_t\theta_W = a_{pt}\theta_P. \quad (16)$$

The a-terms in Eqs. (9), (10), and (16) represent the combined effect of diffusion and convection. The details of these transformations can be found in [10,11].

4. Boundary conditions

4.1. Inlet

In the present study, the jet velocity distribution at the slot-jet exit plane is assumed to be uniform. Thus, at the upper wall, $R = R_1$, the velocity and the thermal boundary conditions are as follows:

for $0 \leqslant \phi \leqslant \varphi$,

$$U = \cos\phi, \quad V = -\sin\phi, \quad \theta = 0, \quad (17)$$

for $\phi > \varphi$,

$$U = V = \theta = 0. \quad (18)$$

The impingement surface, the lower wall, is stationary and impervious and hence $U = V = 0$ at all locations. Due to isothermal conditions at this surface, the non-dimensional temperature is set to $\theta = 1$.

4.2. Outlet

As previously stated, the outlet boundary is located far enough downstream so that the flow conditions are substantially developed. Therefore, for all geometric configurations, the outlet exists at the flat channel section of the solution domain. Accordingly, the following conditions are to be satisfied at the channel outlet:

for $R_1 \leqslant Y \leqslant R_2$,

$$U = \frac{\partial V}{\partial X} = \frac{\partial\theta}{\partial X} = 0. \quad (19)$$

4.3. Plane of symmetry

Symmetric conditions are imposed on the plane over the slot-jet axis. Namely at the symmetry axis,

$$V = \frac{\partial U}{\partial \phi} = \frac{\partial \theta}{\partial \phi} = 0. \tag{20}$$

The mathematical modeling of the aforementioned jet-impingement flow is characterized by four dependent variables and these are the velocity components U and V, the pressure P and the temperature field θ. The total number of finite-difference equations to be solved is equal to the number of dependent variables multiplied by the number of finite-difference cells in the flow domain. Together with the appropriate boundary conditions, the resulting algebraic equations (9), (10), and (16), and the continuity relation are sufficient to solve for the dependent variables at each cell. The numerical procedure employed to perform this task is described next.

5. The numerical solution procedure

The above-derived governing equations are coupled and non-linear due to the fact that the coefficients are functions of the dependent variables themselves. The solution is usually obtained after a number of iterations, and by re-evaluating the values of the coefficients at every iteration. In the present study, the numerical solution is based on the well-known SIMPLER pressure correction algorithm of Patankar [12]. The dependent variables are solved on a line-by-line basis by the tri-diagonal matrix algorithm (TDMA). While solving for a particular variable on a line located at a particular angle of ϕ, the values of this variable on both sides of the line are kept unchanged. This is repeated for all variables of momentum before the next line at $\phi + \delta\phi$ is visited, and at $\phi = 90°$ coordinate transformation is done. Such an iterative method of solution continues until the differences between the new and the old values of the guessed pressure field P^*, and the guessed velocity components satisfy the following convergence criteria at all grid points [13]:

$$\left|P^*_{\text{new}} - P^*_{\text{old}}\right|_P \leqslant 0.001, \quad \left|U^*_{\text{new}} - U^*_{\text{old}}\right| \leqslant 0.005 \quad \text{and} \quad \left|V^*_{\text{new}} - V^*_{\text{old}}\right| \leqslant 0.005. \tag{21}$$

Computing the values of pressure correction, the pressures and the velocities are corrected. After evaluating the corrected velocity field, a computational loop gets completed. For an acceptable solution however the difference between the mass flow rates evaluated at the slot exit and at the channel outlet must be less than 1%. Otherwise, underrelaxation is applied and the velocity components of a particular node P are assumed to be

$$U = U_{\text{old}} + \alpha(U_{\text{new}} - U_{\text{old}}), \quad V = V_{\text{old}} + \alpha(V_{\text{new}} - V_{\text{old}}), \tag{22}$$

where α is the underrelaxation factor and is assumed to be 0.5 in computations. The previous velocity values of all nodes are replaced by the values calculated by Eq. (22). Then the a-terms of equations of motion are recalculated and the entire computational loop is repeated. The computations terminate and the results are recorded if the criterion mentioned above is satisfied repeatedly for each of the subsequent 50 runs.

Using the results of computed velocity field in evaluating the a_t-terms of the energy equation, a similar method of solution is followed. After completion of a computational loop, the difference between the new and the old temperatures has been checked, and at a particular grid, this difference must be less than 0.001. Besides, an energy balance for the entire solution domain is formulated and checked. Thus, to provide a solution to the temperature field, the difference between the energy flow into and out of the channel must be less than 10%. Therefore, considering the recently evaluated temperature field, the iterative computations are maintained until the above-stated two conditions are satisfied.

In addition to the procedure explained above, to provide meaningful results, the optimum size of the grid system has to be determined. A typical effect of the radial direction grid size on heat transfer at the impingement surface is presented by the lower curves in Fig. 5. Increasing the number of grid lines from 100 to 135, especially in the wall jet region, a maximum of 21%

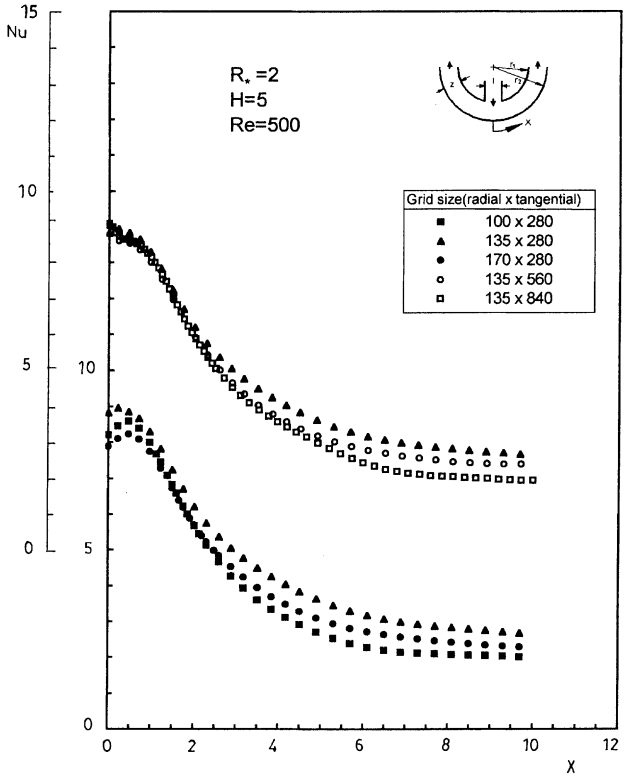

Fig. 5. Influence of finite-difference grid size on Nusselt number variation along the impingement surface.

deviation on the wall heat transfer is noticed. Because of the indiscernible effect at smaller mesh size, however, the number of grid lines in the radial direction is taken to be 135 in this paper. For the angular direction grid size, the upper curves in Fig. 5 indicate the effect of three different grid sizes on the lateral distribution of the wall Nusselt number. It is clear from this figure that the coarse grids used show results that have substantial grid effects, and lack of accuracy. For the flow geometry studied in Fig. 5, the exploratory computations with 20, 40 and 60 grids per computational zone reveal that results are accurate to 2% if the size of the angular increment is less than 0.1°. Hence, depending upon the blow-angle of a particular geometry, for each computational zone, the number of grid lines on the angular direction is varied between 60 and 100 and the total number between 840 and 1400 accordingly.

6. Experimental results

The heat flux, the surface temperature and the pressure data are reduced by a digital computer program and the distribution of the wall static pressure along the impingement surface for two different Reynolds numbers is presented in Fig. 6 as a function of distance from the stagnation point. In this figure, P_r represents the reduced pressure normalized with respect to pressure differential between the stagnation and the end section of the cylindrical channel and is defined as

$$P_r = \frac{P - P_{\phi=90^\circ}}{P_o - P_{\phi=90^\circ}}. \tag{23}$$

At low height ratios, $H \approx 2.2$, and for arc lengths at $1.5 < X < 4$, the existence of negative P_r-values, and a slight increase in pressure gradient along the flow direction are noted. The existence of such subatmospheric regions on the impingement surface for Reynolds numbers greater than 2700 is also observed by Baydar [14]. In Fig. 6, at $Re = 3650$, the pressure becomes subatmospheric approximately at $x/l = 1.5$ and approaches the atmospheric value at $x/l = 4.0$. This in turn indicates the occurrence of a recirculatory zone in the flow field. The recirculatory region becomes stronger with increasing Reynolds number and decreasing height ratio. The existence of a positive pressure gradient field, however, disappears as the channel height increases.

In heat transfer measurements, a preliminary test was undertaken for checking the accuracy of the instrumentation used and validating the procedure applied in collecting the data. To do this, the correlation stated by Gau and Chung [7] for the average Nusselt number of

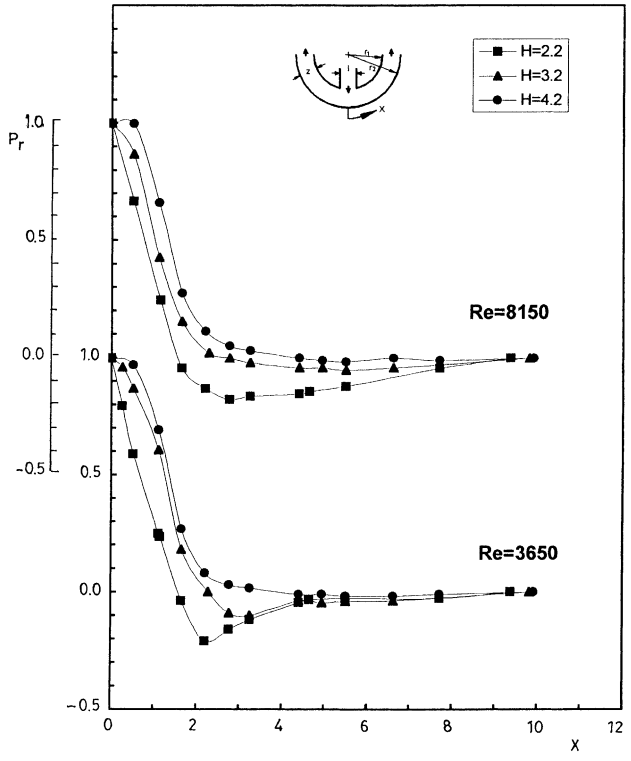

Fig. 6. Effect of height and Reynolds number on impingement surface pressure distribution.

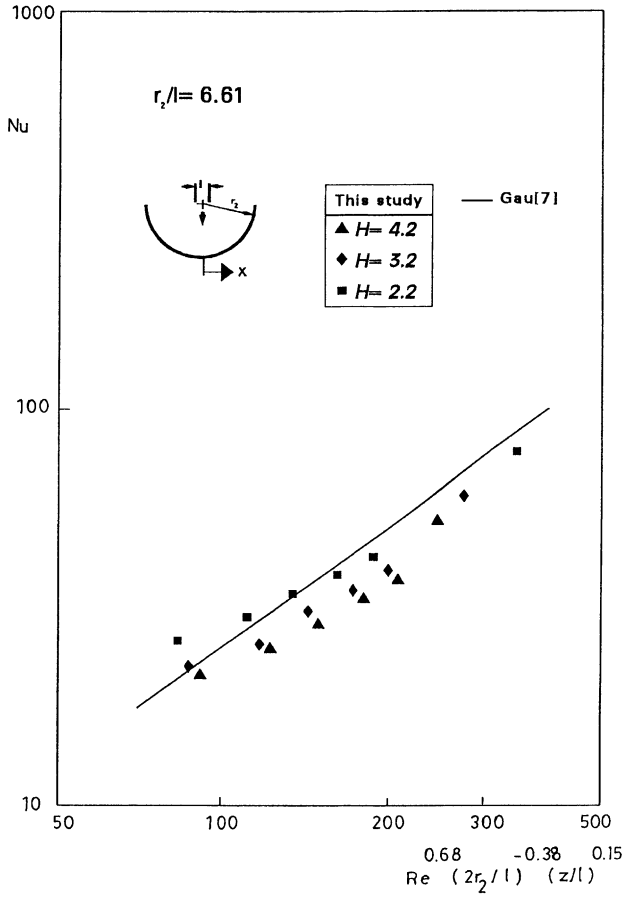

Fig. 7. Comparison of impingement surface heat transfer rates with Gau et al. correlation.

the free-slot-jet impinging on the concave surface is reproduced for a particular geometry of $r_2/l = 6.61$. Measuring the heat transfer rates with the heat flux gages, the average heat transfer coefficients over the impingement surface were calculated. As shown in Fig. 7, the data so obtained for all height ratios were compared with the correlation and the agreement was deemed satisfactory.

The distribution of the local heat transfer on the heated surface of concave channel is given in Fig. 8 as a function of lateral distance from the stagnation point. Three different slot-to-target surface spacings of H, and two Reynolds numbers of 3650 and 8150 for the 12.7 mm-wide slot are illustrated. All curves in Fig. 8 are bell shaped with the maximum value occurring near the stagnation point. For a typical jet Reynolds number, an increase in H causes a decrease in the stagnation heat transfer coefficient, h_o, at a fixed curvature. The effect of H on heat transfer, however, is not traceable for lateral distances greater than four slot widths and a monotonous decrease of heat transfer distribution is observed.

In the stagnation region where the fluid injected through the slot impinges on the heated surface and spreads laterally in a symmetrical fashion, the heat transfer is solely determined by the jet Reynolds number, and the channel height ratio. The dependence of the

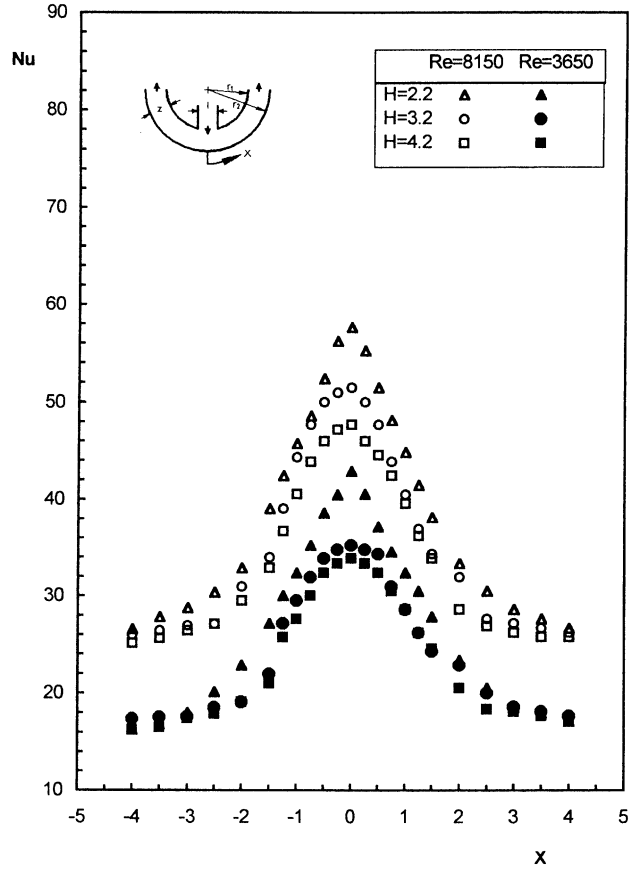

Fig. 8. Variation in the experimentally measured local Nusselt number distribution with channel height and jet Reynolds number.

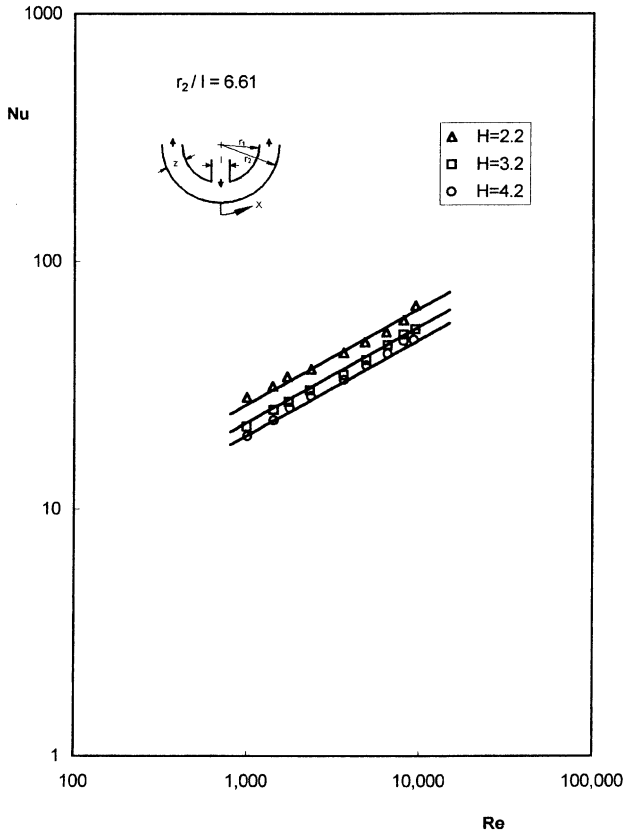

Fig. 9. Effect of channel height on stagnation region heat transfer.

stagnation Nusselt number on these parameters is illustrated in Fig. 9. Applying the least squares curve fit analysis to a total of 30 data points, the stagnation point heat transfer is well correlated as follows:

$$Nu = 2.6Re^{0.386}H^{-0.445}. \tag{24}$$

The above correlation is valid for $1000 \leqslant Re \leqslant 10\,000$, $2.2 \leqslant H \leqslant 4.2$, and $1.5 \leqslant R_* \leqslant 2.75$. The thermophysical properties in Eq. (24) are evaluated at the air inlet bulk temperature. As shown in Fig. 9, the stated correlation represents the data points with a maximum scatter of $\pm 5\%$.

7. Numerical results and discussion

As the preliminary step, the channel radius ratio, R_*, is taken to be very close to unity, i.e., $R_* = 1.01$. In accord with Eq. (1), then the channel curvature becomes very small and a basis is formed to compare the present solution method with the flat channel results. At $H = 4$, the distribution of local heat transfer is provided for the semi-confined jet. Fig. 10 presents such a comparison for flat velocity profile at the slot exit. As evidenced by the general bell-shaped distribution, the non-dimensional heat transfer of the flat channel reproduced at Reynolds numbers of 450 and 950 agrees reasonably well with the data of literature. The results of Miyazaki [2] as ob-

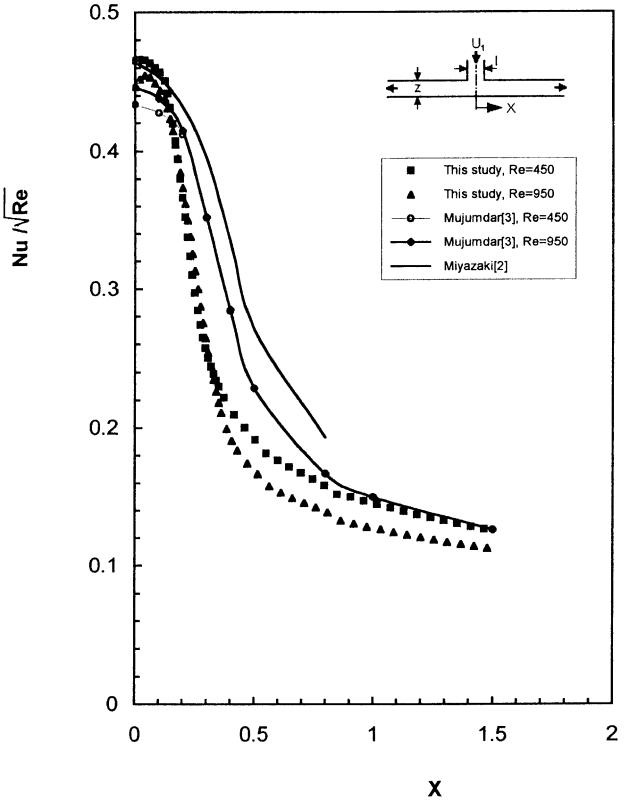

Fig. 10. Model validation by reproducing the flat channel heat transfer results of the literature.

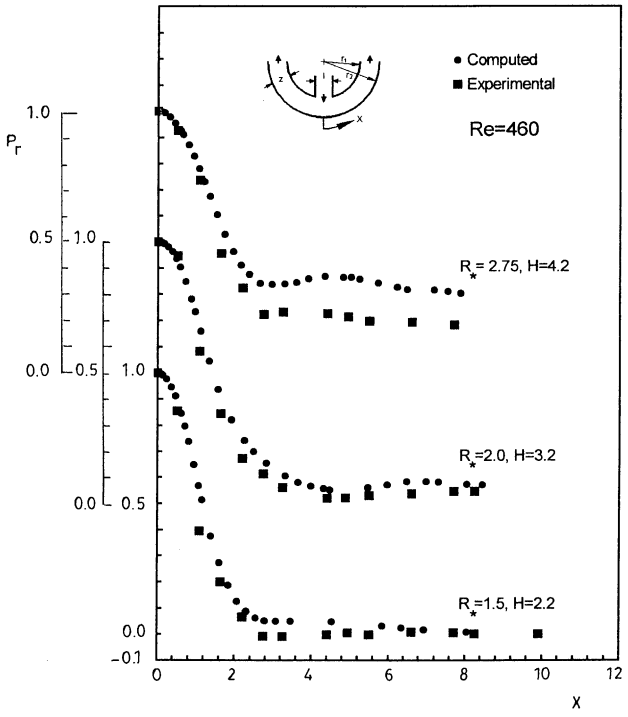

Fig. 11. Comparison of computed and experimental reduced pressure data of the impingement surface at three different flow geometries.

tained by the boundary layer analysis to a free-slot-jet impinging normally on a flat plate describe a maximum of 30% deviation. Due to difference in flow boundary conditions, however, free jet heat transfer data always represent an upper bound to the results of confined jet and such a deviation is expected to take place.

At low Reynolds numbers, a comparison of the numerically determined reduced pressures with the experimental counterparts is provided in Fig. 11. Except the case studied for the height ratio of 4.2, both the numerical and the experimental results agree reasonably well, and in the wall jet region, a slight increase in the pressure gradient along the flow direction is noted. At $H = 4.2$, although both results represent a similar trend, the numerical solution overestimates the data by a maximum of 35% deviation in the wall jet region.

The comparison of the local heat transfer rates for $Re = 460$ at the channel lower surface is provided in Fig. 12. For the height ratios studied, the experimental data and the numerical results coincide reasonably well for arc lengths greater than one-slot-width. For $x/l \leqslant 1$, the stagnation region, the experimental data being higher, a scatter in deviation ranging between 13% and 28% is noticed. Referring to the flow measurements of Choi et al. [15], near the slot exit, there are no velocity fluctuations near the center of the jet. As the jet expands to higher channel heights, however, the mixing of the laminar jet and the ambient air results in velocity fluc-

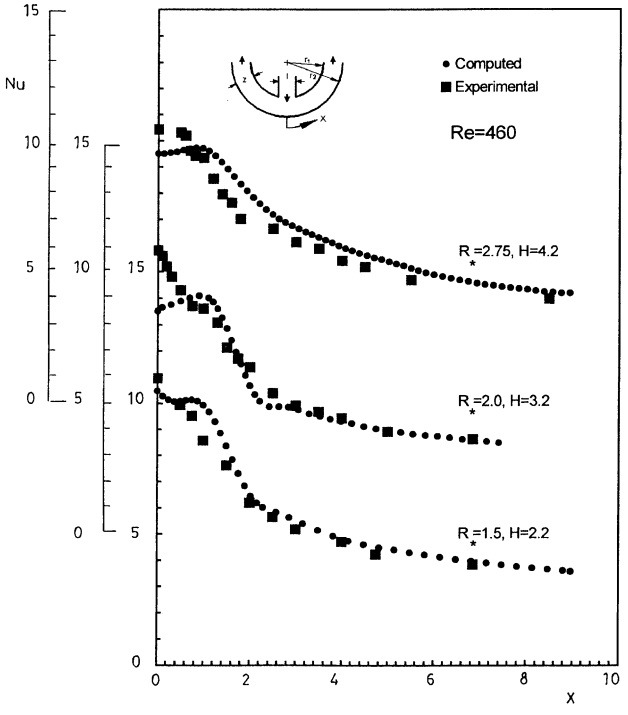

Fig. 12. Comparison of computed and experimental heat transfer data of the impingement surface at three different flow geometries.

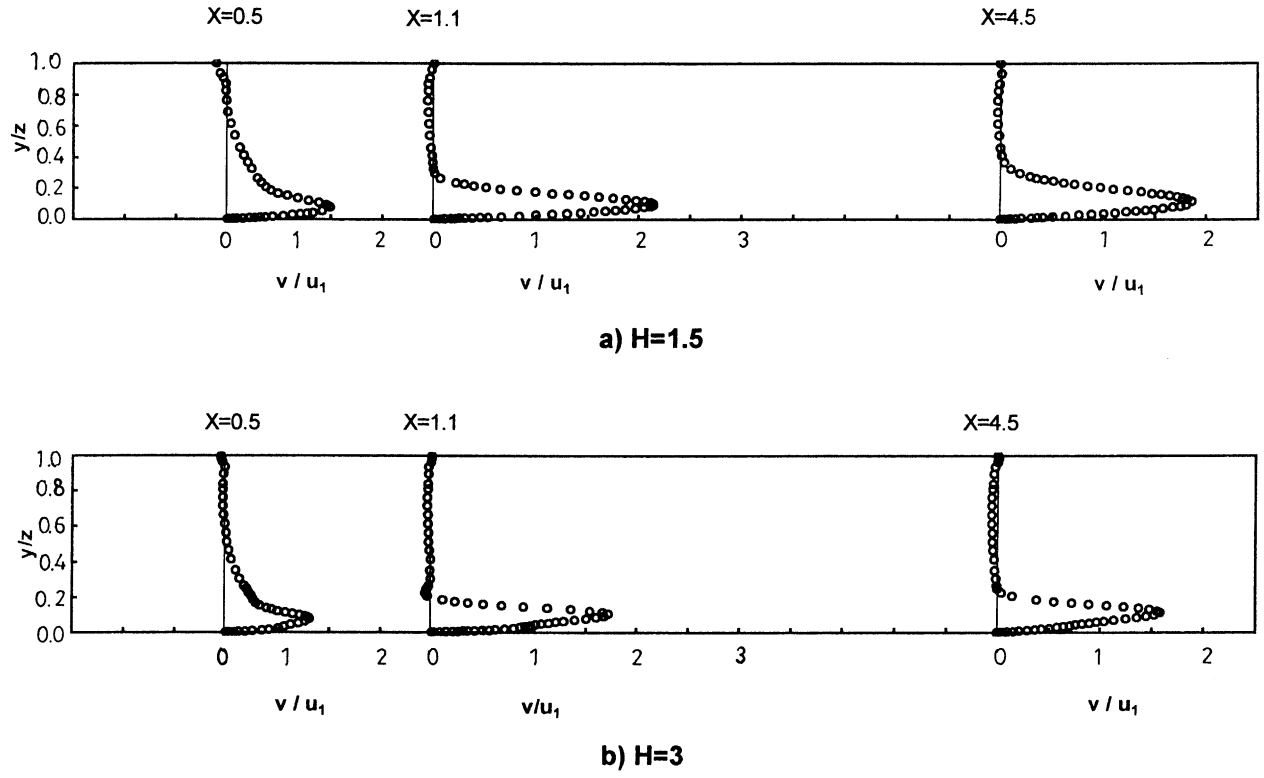

Fig. 13. Streamwise velocity variations across the concave channel at $Re = 600$.

tuations which in turn cause enhancement in local heat transfer rates in the stagnation region.

In Fig. 13, the distributions of the circumferential component of the velocity are provided for two different channel height ratios of 1.5 and 3.0 at $Re = 600$. The values of X on the upper parallel coordinate in Fig. 13 designate the origin of the results for each X; for instance, the line for $X = 4.5$ is the origin of the velocity distribution at $X = 4.5$ where v/u_1 is zero. For the case of $H = 1.5$, Fig. 13(a), the fluid acceleration is observed, and at $X = 1.1$, the peak velocity assumes a maximum and exceeds the nozzle exit velocity by 120%. The peak velocity occurs very close to the surface at $y/z = 0.0988$. At the downstream region of the channel, however, the flow is decelerated and the velocity profile becomes bulky. This behavior of the flow is in accord with the typical pressure distributions in Fig. 11. As shown in Fig. 13(b), at a higher channel spacing of 3.0, the effect of fluid acceleration is less pronounced, and the velocity profiles are bulkier than the ones at $H = 1.5$. However, the arc length location where the peak velocity assumes the maximum is approximately the same as for $H = 1.5$.

Defining the local friction coefficient of the impingement surface as

$$C_f = \frac{2(\sigma_{r\phi})_{wall}}{\rho u_1^2} = \left(\frac{2}{Re}\right)\left(\frac{V(n,j)}{\delta R(n)/2}\right) \tag{25}$$

the effects of the channel curvature and the height on C_f at $Re = 500$ are shown in Fig. 14. For all curves in this figure, since there is no velocity gradient at the point of impingement, the friction factor is zero. In the immediate vicinity of this point, a linear increase in C_f is noticed. At the downstream section, the flow transforms

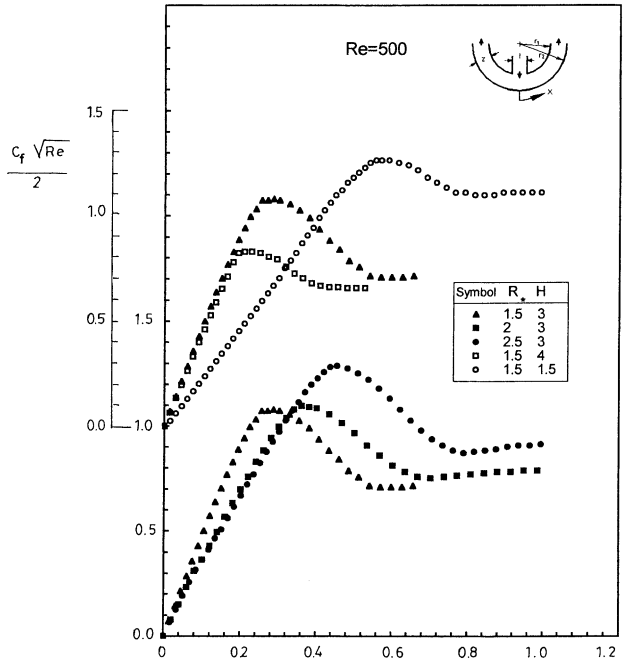

Fig. 14. Effect of channel height and radius ratio on impingement surface friction at $Re = 500$.

into a flow through a channel, and as the limit, the friction should attain the same value as that for two parallel plates having identical channel geometries. In Fig. 14, for a particular radius ratio of 1.5, increasing the channel height decreases the value of the maximum skin friction. This is consistent with the streamwise velocity distribution near the stagnation region. Because of vigorous air entrainment at larger channel heights, the jet flow developed from the edge of the slot exit expands and the boundary layer developed in the stagnation region becomes thicker. As described by the lower curves in Fig. 14, the effect of channel radius ratio on skin friction is not as intense as the effect of channel height. However, increase in channel curvature due to increase in R_* strengthens the centripetal effect on skin friction and the location of $(C_f)_{max}$ shifts away from the point of impingement.

Fig. 15 presents a typical heat transfer distribution along the impingement surface of the channel. The local heat transfer at a particular arc length is determined as

$$Nu(j) = \frac{1-\theta(n,j)}{(\delta R(n)/2)}. \tag{26}$$

The effect of channel height on the lateral variation of heat transfer is shown by the upper curves in Fig. 15. The Nusselt numbers evaluated at the impingement surface are for a fixed Reynolds number of 500 and a fixed channel radius of $R_* = 1.5$. At smaller channel heights, not only are the heat transfer rates enhanced but also the occurrence of the maximum shifts away from the stagnation point. The lower curves in Fig. 15 illustrate the effect of channel radius on the lateral variation of heat transfer and the Nusselt number results are presented for the channel radius ratios of $R_* = 1.5$, 2, and 2.5 at $H = 3$. For the stagnation region, $x/l < 1$, no appreciable change in the overall distribution of heat transfer is noticed. In the wall jet region, however, an enhancement in heat transfer due to increase of curvature takes place. Such an elevation in the Nusselt numbers is attributed to the initiation of a series of Taylor–Görtler vorticies that extend over the entire surface. For flow over a concave surface, a centrifugal force generated due to the curvature can destabilize the flow and lead to the type of instability that is referred to as the Taylor–Görtler vortex. It has been determined by Mayle et al. [16] that the generation of such vortices can significantly increase the momentum and energy exchange in the flow and enhance the heat transfer along the wall.

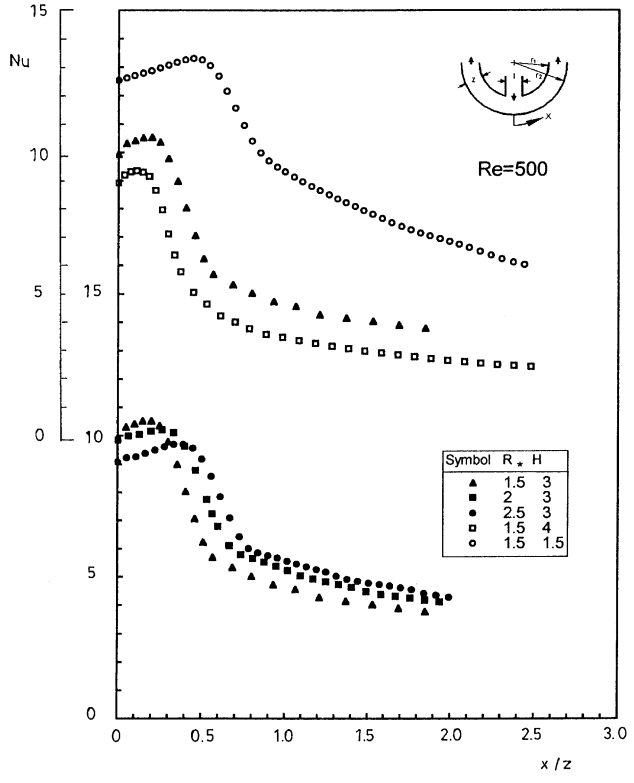

Fig. 15. Effect of channel height and radius ratio on lateral distribution of heat transfer at $Re = 500$.

8. Practical significance/usefulness

In addition to the studies related to two-dimensional free jet flow over a concave surface, this study considers a semi-confined slot-jet issuing into a concave channel at the symmetry line, and predicts the heat transfer characteristics of the flow by varying the height and the Reynolds number of the channel. Within the limits of the parameters studied, a correlation is stated for the stagnation region heat transfer. Considering the engineering importance, the lateral distributions of surface pressure and heat transfer rates are illustrated. A numerical model is developed and provides a basis for further study in predicting the flow behavior at high Reynolds numbers.

9. Concluding remarks

An experimental test set-up has been built for measurements of flow and heat transfer characteristics of confined slot-air-jet flowing through a semi-circular concave channel. Particular emphasis in experimental runs has been placed on determining the effect of the channel height and the Reynolds number on impingement surface pressure and heat transfer distributions. The flow Reynolds number is varied in the range between 200 and 11 000. For flow conditions at $Re \geqslant 1000$ and $H = 2.2$, a subatmospheric region occurs on the impingement surface, and this region becomes stronger with the increase of Reynolds number. The heat transfer measurements at the stagnation region indicate that Nusselt number is not affected by the variation of the channel radius ratio. However, in accord with the results of Choi et al. [15], the Nusselt number at the stagnation region decreases as the channel spacing increases from 2.2 to 4.2. For a scatter of ±5%, the Nusselt number data

of the stagnation region are well correlated with the jet Reynolds number, Re, and the channel height ratio, H.

A mathematical model for predicting the steady and laminar behavior of the flow is constructed. Referring to the experimentally measured velocity data, a uniform velocity profile is assumed to exist at the slot exit in the numerical analysis. The computational results are compared with the experimental counterparts at $Re = 460$. For the geometric cases studied, a reasonably good agreement on pressure data is attained. However, in comparing the circumferential Nusselt number variations, specifically at the stagnation region, a maximum of 28% deviation between the experimental and the computed data is noted. Due to penetration of jet velocity fluctuations into the potential core region of the slot-jet, experimentally higher values of heat transfer rates around the stagnation region are expected to occur. The surface pressure measurements indicate the existence of a high velocity wall jet at the channel surface. This result is consistent with the numerically computed velocity profiles of the wall jet. In the numerical analysis, the geometric parameters of the flow were varied in the range between $1.5 \leqslant R_* \leqslant 2.5$ and $1.5 \leqslant H \leqslant 5.0$ so that the channel curvature ζ assumed values between 0.2 and 1.0. An increase in channel curvature improves the overall heat transfer distribution on the impingement surface of the channel. Due to velocity fluctuations of wall jet flow along the concave surface, numerical solutions present instability at high Reynolds numbers. Hence, the flow Reynolds number in the numerical analysis assumed values up to 600.

Acknowledgements

The authors would like to acknowledge the financial assistance provided by the University Research Funds under the grant no. 0922.97.01.43.

References

[1] R. Gardon, J.C. Akfirat, Heat transfer characteristics of impinging two-dimensional air jets, J. Heat Transfer, Trans. ASME 88 (1966) 101–108.

[2] H. Miyazaki, E. Silberman, Flow and heat transfer on a flat plate normal to a two-dimensional laminar jet issuing from a nozzle of finite height, Int. J. Heat Mass Transfer 15 (1972) 2097–2107.

[3] A.R.P. Van Heiningen, A.S. Mujumdar, W.J.M. Douglas, Numerical prediction of the flow and impingement heat transfer caused by a laminar slot jet, J. Heat Transfer, Trans. ASME (1976) 654–658.

[4] K. Ichimiya, N. Hosaka, Experimental study of heat transfer characteristics due to confined impinging two-dimensional jets, in: Proceedings of Second World Conference on Experimental Heat Transfer Fluid Mechanics and Thermodynamics, Elsevier, Amsterdam, 1991, pp. 771–775.

[5] D.E. Metzger, T. Yamashita, C.W. Jenkins, Impingement cooling of concave surfaces with lines of circular air jets, J. Eng. Power, Trans. ASME 91 (3) (1969) 149–158.

[6] R.K. Brahma, I. Padhy, B. Pradhan, Prediction of stagnation point heat transfer for a slot-jet impinging on a concave semi-cylindrical surface, in: Wärme und Stoffübertragung, vol. 24, Springer, Berlin, 1989, pp. 1–8.

[7] C. Gau, C.M. Chung, Surface curvature effect on slot-air-jet impingement cooling flow and heat transfer process, J. Heat Transfer, Trans. ASME 113 (1991) 858–864.

[8] G. Yang, M. Choi, J.S. Lee, An experimental study of slot jet impingement cooling on concave surface: effects of nozzle configuration and curvature, Int. J. Heat Mass Transfer 42 (1999) 2199–2209.

[9] H. Schlichting, Boundary-Layer Theory, seventh ed., McGraw-Hill, New York, 1979.

[10] S.V. Patankar, Numerical Heat Transfer and Fluid Flow, Hemisphere, New York, 1980.

[11] W.J. Minkowycz, E.M. Sparrow, G.E. Schneider, R.H. Pletcher, Handbook of Numerical Heat Transfer, Wiley, New York, 1988 (Chapter 6).

[12] S. Küçüka, Effect of curvature on two-dimensional impingement cooling, Ph.D. Thesis, Department of Mechanical Engineering, Dokuz Eylul University, Izmir, Turkey, 1993.

[13] N. Kim, N.K. Anand, D.L. Rhode, A study on convergence criteria for a simple-based finite-volume algorithm, Numer. Heat Transfer, Part B 34 (1998) 401–417.

[14] E. Baydar, Confined impinging air jet at low Reynolds numbers, Exp. Therm. Fluid Sci. 19 (1999) 27–33.

[15] M. Choi, H.S. Yoo, G. Yang, J.S. Lee, D.K. Sohn, Measurements of impinging jet flow and heat transfer on a semi-circular concave surface, Int. J. Heat Mass Transfer 43 (2000) 1811–1822.

[16] R.E. Mayle, M.F. Blair, F.C. Kopper, Turbulent boundary layer heat transfer on curved surfaces, J. Heat Transfer, Trans. ASME 101 (1979) 521–525.